crystals

MDPI

Article

Synthesis and Crystal Structure of $Zr_3V_3GeSn_4$

Daniel Parks †, Karim Niang, Yuri Janssen and Jack W. Simonson *

Department of Physics, Farmingdale State College, Farmingdale, NY 11735, USA
* Correspondence: jack.simonson@farmingdale.edu
† Current address: Department of Mechanical Engineering, Stony Brook University, Stony Brook, NY 11794, USA.

Abstract: Quantum fluctuations inherent in electronic systems positioned close to magnetic instabilities can lead to novel collective phenomena. One such material, β-Ti_6Sn_5, sits close to ferromagnetic (FM) instability and can be pushed to an itinerant FM-ordered state with only minute magnetic or non-magnetic doping. The binary nature of this compound, however, limits the tuning variables that can be applied to study any emergent physics, which are likely to be sensitive to the introduction of chemical disorder.Accordingly, we grew high-quality single crystals of a new quaternary compound $Zr_3V_3GeSn_4$ from a Sn-rich self flux, and determined the structure with single-crystal X-ray diffraction. $Zr_3V_3GeSn_4$ forms in an ordered derivative of the hexagonal β-Ti_6Sn_5 structure with Zr and V atomic positions that show no indication of site interchange. Ge likewise occupies a single unique atomic position. The V site, which would be the one most likely to give rise to any magnetic character, is located at the center of a distorted octahedron of Sn, with such octahedra arranged in face-sharing chains along the crystallographic **c** axis, while the chains themselves are organized in a kagome geometry. $Zr_3V_3GeSn_4$ represents the second known quaternary phase within this system, suggesting that other compounds with this structure type await discovery.

Keywords: flux growth; X-ray diffraction; ordered derivative; crystal structure; transition metal intermetallics

check for updates

Citation: Parks, D.; Niang, K.; Janssen, Y.; Simonson, J.W. Synthesis and Crystal Structure of $Zr_3V_3GeSn_4$. *Crystals* **2023**, *13*, 744. https://doi.org/10.3390/cryst13050744

Academic Editors: Andrei Vladimirovich Shevelkov and Andrey Prokofiev

Received: 30 March 2023
Revised: 14 April 2023
Accepted: 27 April 2023
Published: 29 April 2023

Copyright: © 2023 by the authors. Licensee MDPI, Basel, Switzerland. This article is an open access article distributed under the terms and conditions of the Creative Commons Attribution (CC BY) license (https://creativecommons.org/licenses/by/4.0/).

1. Introduction

Interactions between electrons and magnetic fluctuations within correlated systems can often yield unexpected properties, including superconductivity [1], metal insulator transitions [2], half-metallicity [3], and coupled spin dimers [4]. Given this diversity of phenomena, there are relatively few known itinerant ferromagnetic systems, with $ZrZn_2$ and Sc_3In being perhaps the most famous due to their potential proximities to quantum critical points (QCPs) [5–7], though others exist, including in atomically thin systems [8,9]. In such systems, it appears that an eventual ferromagnetic quantum critical point (FM-QCP) can be reached by chemical substitution [10–12]. On the other hand, a FM-QCP in clean metals is often instead preempted by the emergence of another collective phase [13–17], although a FM-QCP could potentially be stabilized even in pure systems by a non-centrosymmetric crystal structure [18].

The hexagonal β-phase of Ti_6Sn_5 has been known for decades and forms in the centrosymmetric $P6_3/mmc$ space group [19,20]. This phase is purportedly thermodynamically favored over the orthorhombic-structured α-phase at temperatures $T > 1063$ K [21]. Even at higher temperatures, however, the β-phase sits just at the cusp of stability with even high-quality single crystal samples containing intergrowths of the low-temperature α-phase, which take the form of planar-like stacking faults within single crystallites [22]. The hexagonal phase can nonetheless be stabilized both above and below the virgin transition temperature with the addition of impurities [23,24]. Furthermore, and perhaps most interestingly, the presence of impurities —magnetic or otherwise – can push β-Ti_6Sn_5 into a ferromagnetic ordered state, indications of which are reported to persist in the pure

compound. Thermodynamic and magnetic measurements [23] reveal a large electronic contribution to the specific heat $\gamma = 40.4$ mJ/mol K^2 and an enhancement of the dimensionless Wilson ratio $R_W = \alpha\chi/\gamma = 1.76$ over the free-electron value of unity, where χ represents the T-independent component of the dc-magnetic susceptibility, and $\alpha = \pi^2 k_B^2/3\mu_B^2$. Careful magnetic characterization of doped β-Ti_6Sn_5 single crystals indicates the onset of ferromagnetic order with the introduction of dopants at very modest molar concentrations corresponding to only 0.025% (magnetic) Ce, 3% (non-magnetic) La, or 3% Co [23]. The onset of the transition with La is presumably an inverse-pressure effect, but curiously neither partially replacing Ti with larger Zr nor partially replacing Sn with likewise larger In or Bi results in observation of the FM ordered phase. Nonetheless, the large Sommerfeld coefficient γ of the pure material is likewise found in density functional theory (DFT) calculations [25], while we remain unaware of any DFT studies of its doped analogs.

The crystal structure of β-Ti_6Sn_5 consists of five distinct atomic positions with Ti occupying two with Wyckoff positions 6*h* and 6*g*, while Sn occupies 6*h*, 2*a*, and 2*c* sites [20]. The existence of multiple inequivalent positions for both Ti and Sn suggests the possibility that each site could be manipulated independently, perhaps even to the extent that each could host a distinct element, and indeed, there have thus far been two reported attempts to produce ternary and quaternary analogs of this compound. The first report produced three isotypic compounds of the form RE_3RuMg_7, where RE = Sm, Gd, or Tb, and presented the crystal structure of $Sm_{3.16(1)}RuMg_{6.84(1)}$ [26]. Here, Sm fully occupies the 6*h* Ti site of β-Ti_6Sn_5, Mg occupies the 6*h* Sn and 6*g* Ti sites, Ru occupies the 2*a* site, and the 2*c* site consists of a mixture of Sm and Mg. Magnetic properties of these rare earth-bearing phases have not been reported to our knowledge. More recently, a first quaternary analog of β-Ti_6Sn_5 appeared in the crystallographic literature: $Zr_3Mn_3Sn_4Ga$, which bears linear chains of Mn [27]. Here, the chains are arrayed in kagome geometry with Mn–Mn distances of 2.81435(11) Å along the chain direction and 4.6037(3) Å between neighboring chains.

Taking these multinary analogs as inspiration, we report in the present work the single-crystal synthesis and crystal structure of a new intermetallic compound $Zr_3V_3GeSn_4$, which takes the same structure-type as $Zr_3Mn_3Sn_4Ga$. Here, the two Ti sites of β-Ti_6Sn_5 are separately occupied by Zr and V, while the Sn 2*b* site is occupied by Ge. The existence of now two quaternary ordered derivatives of β-Ti_6Sn_5 suggests that a wealth of undiscovered systems may exist within this structure-type—likely having compositions similar to $Zr_3M_3BSn_4$, for 3*d* transition metal *M* and *B*-group element *B*—thus enabling a new levers to tune the magnetic properties of compounds structurally related to β-Ti_6Sn_5.

2. Materials and Methods

2.1. Crystal Growth

We grew high-quality single crystals of $Zr_3V_3GeSn_4$ from a Sn-rich solution. The initial constituents were solid pieces of pure elements obtained commercially: 99.999% Ge ingot from Strategic Metal Investments, 99.99+% Sn shot from Alfa Aesar, 99.7% V turnings from Alfa Aesar, and 99.8% Zr lump from Alfa Aesar. These pieces were combined with an atomic ratio of 10:1:0.5:88.5 Zr:V:Ge:Sn. We loaded these constituent elements into Al_2O_3 crucibles, which we then placed into clear, fused quartz tubing that we evacuated, backfilled with 30 kPa of ultra high purity Ar gas, and subsequently sealed to form ampoules. We heated the sealed ampoules to 1323 K at a constant ramp rate of 650 K/h over a period of 2 h, held them at that temperature for another 2 h, and slowly cooled at a constant rate of 4.53 K/h to 1033 K over a period of 64 h. We removed the ampoules from the furnace at 1033 K and quickly decanted the molten solution by spinning the sealed ampoules in a centrifuge at 2000 rpm for 60 s. Upon opening the ampoules, we observed the crystals to take the form of rods of elongated hexagonal habit and silvery metallic luster with lengths up to several millimeters.

2.2. Analytical Methods

We carried out X-ray diffraction measurements on a ∼40 µm × ∼50 µm × ∼460 µm rod-shaped crystal at $T = 293$ K using a four-circle Oxford Gemini single-crystal diffractometer equipped with a two-dimensional Atlas CCD plate detector. The X-ray wavelength was 0.71073 Å from a Mo-Kα source, the energy was 1.6 kW, and the beam was collimated to 500 µm. We measured some 65,061 reflections corresponding to 99.9% completeness from $4.42^\circ \leq \theta \leq 45.58^\circ$ providing access to the span of Miller indices $-18 \leq h \leq 18$, $-18 \leq k \leq 18$, $-11 \leq l \leq 11$. We computed the sample absorption correction numerically using a multifaceted crystal model [28] with $T_{min} = 0.047$ and $T_{max} = 0.45$. The experimental absorption coefficient $\mu = 22.321$ mm^{-1}.

We carried our least-square refinement of fit parameters using the Jana2006 crystallographic computing system [29] and solved the phase problem using the Superflip charge-flipping algorithm [30]. We visualized the structures with VESTA [31].

Our resulting CIF file appears in the Crystallography Open Database under entry number 3000436: https://www.crystallography.net/cod/3000436.html, accessed on 25 April 2023.

3. Results

3.1. Structural Commentary

Figure 1 depicts several polyhedral representations of the crystal structure of $Zr_3V_3GeSn_4$, highlighting the linear configurations of the V and Ge positions. Figure 1a shows a representation of the structure with the crystallographic **c** axis pointing up, the direction coincident with linear chains of V (red) and separate linear chains of Ge (black). V–V distances are 2.78355(10) Å along the chains, while each V position is coordinated by six Sn (gray) atoms across two independent atomic sites, forming a highly distorted Sn_6 octahedron around each V position. Zr (white) positions fill the gaps among these octahedra.

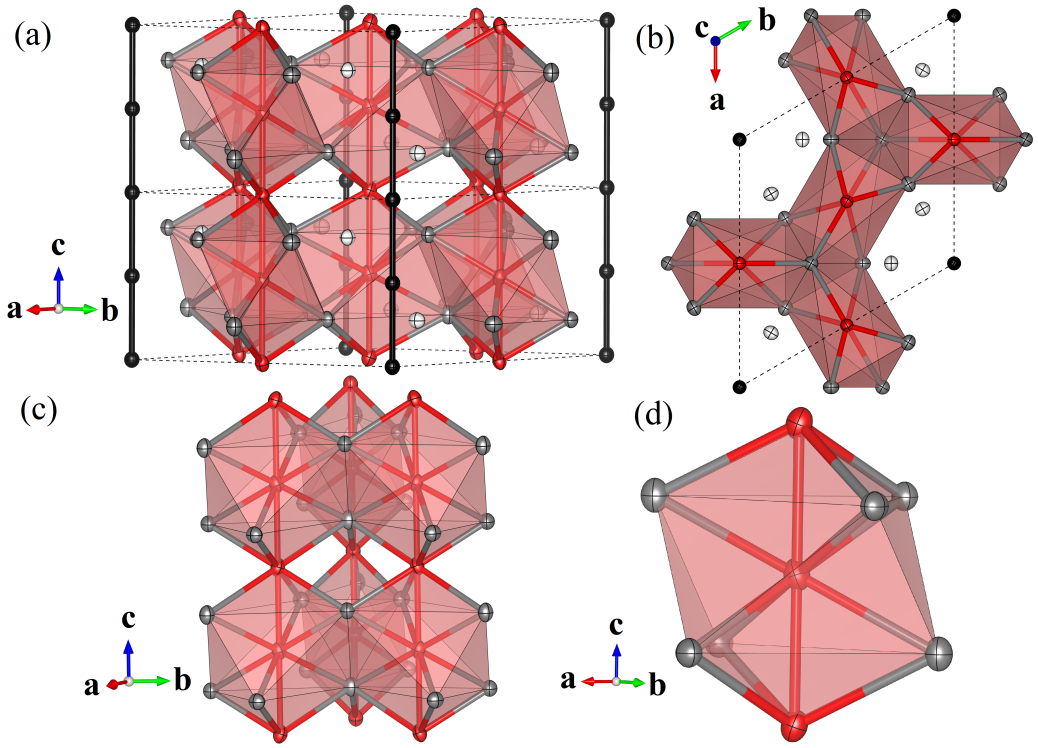


Figure 1. (**a**) The crystal structure of $Zr_3V_3GeSn_4$. Zr is drawn in white, V in red, Ge in black, and Sn in gray. Anisotropic displacement parameters are drawn at the 99% level. (**b**) The crystal cell viewed from down the **c** axis to highlight the triangular arrangement of the linear chains of V. (**c**) Three nearest-neighbor chains of V, showing the orientation of neighboring coordination polyhedra of V. (**d**) The coordination polyhedron of V.

The linear chains of V are themselves arranged in kagome-like triangles within the **ab** plane, as we show via a view directly down the **c**-axis in Figure 1b. The interchain distances between V positions are uniformly 4.61450(11) Å, some 66% longer than the intrachain V–V distances, underscoring that $Zr_3V_3GeSn_4$ cannot be understood as a system of isolated, two-dimensional kagome planes, but instead the fundamental building block is linear chains along **c** that are then arranged into triangles. This idea is clarified in Figure 1c, which depicts the mutual orientations of three neighboring chains of V positions and the associated polyhedra.

Figure 1d provides a closer look at the V-centered polyhedra, which are distorted VSn_6 octahedra, stacked along **c** and mutually face-sharing. The central V has four Sn nearest neighbors with V–Sn distances 2.75791(16) Å. Its next-nearest neighbors are V atoms along the chain direction, and the octahedron is completed with two next-next-nearest-neighbor Sn atoms with V–Sn distances of 3.00581(15) Å.

3.2. Details of Structure Solution

Crystal data, data collection, and structure refinement details corresponding to the model shown in Figure 1 are summarized in Table 1, while structural parameters of the solution are shown in Tables 2 and 3.

Table 1. Crystal data and structural refinement parameters for $Zr_3V_3GeSn_4$.

Parameter	Value
Empirical formula	$Zr_3V_3GeSn_4$
Formula weight	973.9
Collection temperature (K)	294(1)
Wavelength (Å)	0.71073
Space group	P 6_3/m m c (194)
a (Å)	9.2290(2)
b (Å)	9.2290(2)
c (Å)	5.56710(10)
Volume (Å^3)	410.647(19)
Z	2
Calculated density (g/cm^3)	7.8764
Absorption coefficient (mm^{-1})	22.321
F(000)	842
Crystal size (mm)	0.053 × 0.042 × 0.463
θ range of data collection °	4.42–45.48
Index range	$-18 \leq h \leq 18$ $-18 \leq k \leq 18$ $-11 \leq l \leq 11$
Total reflections	65061
Independent reflections	695
R_{int}	0.0507
Completeness to θ_{max}	0.99
Goodness of fit	2.12
Data/restraints/parameters	691/0/18
R_1 (on F_0, $I > 3\sigma(I)$)	0.0156
wR_2 (on F_0, all data)	0.0280

Figure 2 shows unwarped diffraction maps along the (hk0) and (h0l) directions that indicate the high-quality and single-phase nature of the measured crystal. We carefully inspected these unwarped images to verify that no twin domains or modulations were present. We observed no evidence of Bragg reflections due to additional domains, and furthermore blind, computer-automated attempts to index any putative domains yield only trivial rotation matrices relative to the **UB** matrix of the primary domain. Specifically, given

the previous reports of the potential for α- and β-Ti_6Sn_5 intergrowth, we took particular pains to confirm that there was no evidence of an unreported orthorhombic phase coexisting within $Zr_3V_3GeSn_4$. Moreover, the data are clearly devoid of any spurious peaks aside from the expected $\lambda/2$ reflections, and the interstitial regions of the resulting Fourier transform charge density were likewise free of substantial peaks of positive and negative charge in both F_{obs} and F_{calc}.

Table 2. Details of the structure of $Zr_3V_3GeSn_4$.

Site	Wyckoff Pos.	x	y	z	U_{ani} ($\times 10^2$) Å^2
Sn1	2*c*	2/3	1/3	3/4	0.667(7)
Sn2	6*h*	0.786778(14)	0.213222(14)	1/4	0.624(6)
Zr1	6*h*	0.85347(2)	0.14653(2)	3/4	0.591(8)
Ge1	2*a*	0	0	0	0.549(10)
V1	6*g*	1/2	0	1/2	0.586(11)

Table 3. Refined anisotropic displacement parameters of $Zr_3V_3GeSn_4$ (Å$^2 \times 10^2$).

Site	U_{11}	U_{11}	U_{11}	U_{11}	U_{11}	U_{11}
Sn1	0.571(8)	0.571(8)	0.858(13)	0.286(4)	0	0
Sn2	0.573(7)	0.573(7)	0.617(8)	0.204(6)	0	0
Zr1	0.632(9)	0.632(9)	0.579(11)	0.369(9)	0	0
Ge1	0.521(12)	0.521(12)	0.604(18)	0.261(6)	0	0
V1	0.492(13)	0.530(16)	0.750(17)	0.265(8)	0.045(7)	0.090(14)

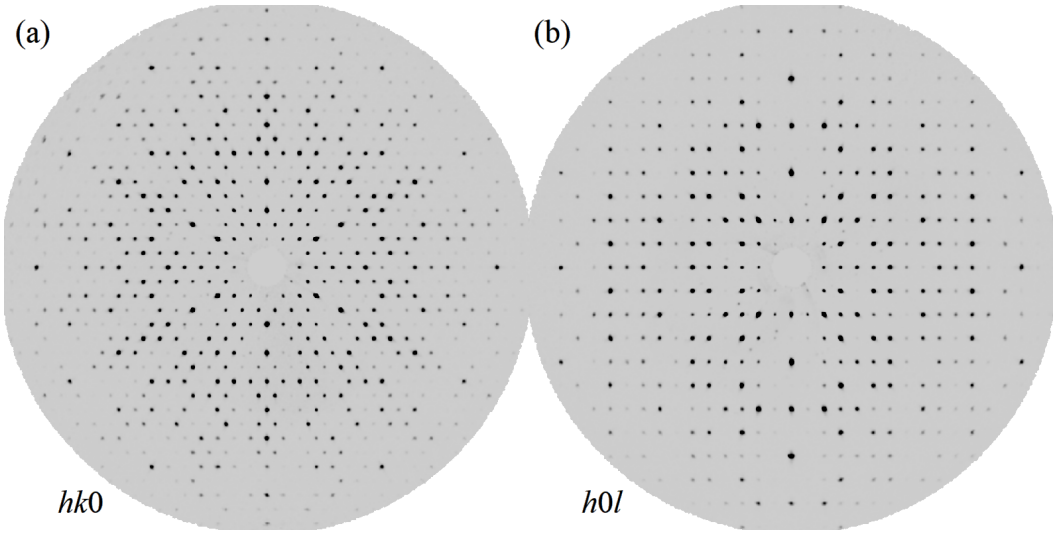


Figure 2. (**a**) The unwarped *hk*0 diffraction plane of $Zr_3V_3GeSn_4$, as indicated, measured out to 0.50 Å and showing absence of non-merohedral twins, superstructures, modulated structures, or systematic unindexed reflections. (**b**) As in (**a**) but the unwarped *h*0*l* plane, as indicated.

After indexing the reflections and identifying systematic absences to determine the unit cell and space group, we assigned atom types based on the the magnitudes of positive charge obtained from the charge-flipping algorithm. We then carried out our refinements of lattice parameters, atomic positions, and isotropic displacement parameters on the structure factors *F*. We observed that subsequently allowing the refinement of anisotropic displacement parameters (ADPs) significantly improves the quality of the refinement. The resulting ADPs are small and realistic, and as we show in Figure 1 and Table 3, displacement tends to prefer the directions normal to those of interatomic bonds, as expected. Given the site mixing reported for $Sm_{3.16(1)}RuMg_{6.84(1)}$ [26], we also carefully considered the possibility of mixed or partial occupancy in $Zr_3V_3GeSn_4$. Permitting partial occupancy on any site or

any combination thereof, however, did not appreciably improve refinement. We therefore conclude that all atomic positions in the structural model are of integer occupancy.

Figure 3 shows that the observed scattering from our crystal is missing intensity for reflections with Miller indices {002}, {004}, {006}, and {008}, relative to the intensities calculated by our structural model. We carefully considered the possibility that this discrepancy was related to a portion of the crystal falling out of the beam in certain orientations during measurement, but this interpretation is inconsistent with the data and the geometry of the crystal. Accordingly, we attempted to model this missing intensity with extinction and found the best extinction model for the data as a whole to be isotropic for a type I crystal with a Gaussian distribution of crystallites [32]. The resulting single, refined extinction parameter $g_{\mathrm{iso}} = 700(40)$. The structure factors shown in Figure 3a,b have already been corrected for isotropic extinction, yet the missing intensity for these the {002n} peaks persists, as indicated in Figure 3a. Nonetheless, including even a single-parameter extinction model significantly improves the quality of the refinement, with the goodness of fit of the observed reflections improving from 5.24 to 2.69 and wR of all reflections improving from 0.0679 to 0.0350. Both values are further improved with manual culling as we discuss below. Nevertheless, extinction is clearly very important to modeling the scattering from this crystal, which is perhaps unsurprising given the presence of heavy elements and the high aspect ratio associated with its rod-like habit.

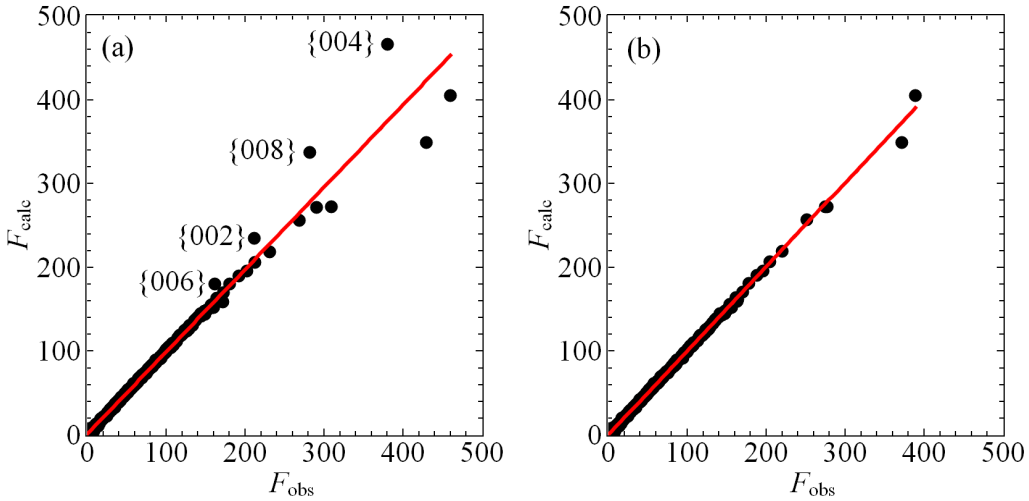


Figure 3. (**a**) A plot of the calculated structure factors F_{calc} plotted against the observed structure factors F_{obs} after correcting for isotropic extinction but prior to culling the reflections corresponding to {002n}, $n \leq 4$, as indicated, the scattering of which are observed to be anomalously low. The solid red line is a line of best fit determined by regression. (**b**) As in (**a**) but after culling, revealing superior agreement between the data and the model, particularly for reflections with large structure factors F.

The missing observed intensities of these peaks led us to consider the possibility that these highest structure factor reflections were so broad that our integration masks blocked a substantial portion of their tails, but doubling the integration mask radii produced little effect on the quality of the refinement, nor did it find meaningful additional intensity for these reflections. We considered that an alternative explanation for the missing F_{obs} could be an inadequate absorption correction. Accordingly, we modified our physical model of the shape of the crystal to be alternatively larger and smaller in both the **ab** and **c** directions, but these changes likewise made no appreciable improvement to the refinement. We also applied the rather unphysical option of overlaying a spherical absorption correction, which is typically done with strongly absorbing samples, but it too produced no improvement.

Ultimately, we elected to cull these reflections from the dataset manually, as we show in Figure 3b. Given that we observe no streaking, no incommensurate peaks, and no evidence for a charge-density wave, there is nowhere else in the structure to account for the missing intensity, while gross errors in the model are unlikely given the low goodness

of fit and residual parameters of the current refinement. We cannot a priori rule out the possibility of inadequately modeled disorder, but we stress that permitting refinement of the occupancies of any combination of atomic sites neither substantially improves the refinement nor addresses the issue of excess localized charge in F_{calc}. We conclude the missing intensity is the result of an anisotropic extinction that we are unable to model adequately. The effects of culling these peaks on the structural parameters shown in Tables 2 and 3 are minimal. Atomic positions are wholly unchanged, and new values of ADPs fall within their uncertainties with a single exception: U_{33} of the Sn2 site is reduced from 0.00640(11) Å^2 before culling to 0.00617(8) Å^2 after culling. We judge this minor discrepancy to be worth an improved fit of the model to the observed scattering on the whole. Therefore, the structural parameters presented in this work represent a model based upon the culled data.

4. Discussion

Table 4 compares the lattice parameters, cell volumes, site occupancies, and any atomic parameters that are not fixed by symmetry among the reported crystal structures of β-Ti_6Sn_5 and its known multinary analogs. This structure type is apparently capable of accommodating a rather wide range of parameters with variations as large as 11% of a and 9% of c permitted. Cell volumes are likewise permitted over a wide range, with the smallest unit cell (that of $Zr_3V_3GeSn_4$ in the present work) occupying only 73% the volume of the largest, $Sm_{3.16(1)}RuMg_{6.84(1)}$. The ratio of the lattice parameters a/c appears to require a narrower window, with only a 4% different between the smallest and largest. Since the atomic positions of the 3*d* transition metals putatively most likely to give rise to magnetism—V in $Zr_3V_3GeSn_4$ and Mn in $Zr_3Mn_3Sn_4Ga$—are fixed by symmetry, the metal-metal distances along the chains in the **c**-direction and within the triangles in the *ab*-plane can be obtained directly from the lattice parameters. The intrachain distance is given by $c/2$, and the intraplanar distance is given by $a/2$. Taken together with the relatively small variations among transiton metal atomic radii, the reported range of these parameters suggests that other isostructural, unreported multinary compounds are likely to exist with this structure type as well.

Table 4. Comparison of the crystal structures of β-Ti_6Sn_5, $Sm_{3.16(1)}RuMg_{6.84(1)}$, $Zr_3Mn_3Sn_4Ga$, and $Zr_3V_3GeSn_4$ at $T \simeq 300$ K.

Parameter	β-Ti_6Sn_5	$Sm_{3.16(1)}RuMg_{6.84(1)}$	$Zr_3Mn_3Sn_4Ga$	$Zr_3V_3GeSn_4$
a (Å)	9.248	10.341(2)	9.2073(4)	9.2290(2)
c (Å)	5.69	6.113(1)	5.6287(2)	5.56710(10)
a/c	1.63	1.6916(4)	1.64577(9)	1.65778(5)
V (Å^3)	421.44	566.1	413.24(4)	410.647(15)
2*c* atom	Sn	$Mg_{0.843(4)}Sm_{0.157(4)}$	Sn	Sn
6*h* atom	Sn	Mg	Sn	Sn
6*h* atom	Ti	Sm	Zr	Zr
2*a* atom	Sn	Ru	Ga	Ge
6*g* atom	Ti	Mg	Mn	V
6*h* x	0.795	0.77352(13)	0.78917(3)	0.786778(14)
6*h* x	0.835	0.86951(2)	0.85295(4)	0.85347(2)
Reference	[20]	[26]	[27]	This work

Similarly to β-Ti_6Sn_5, $Zr_3V_3GeSn_4$ almost certainly represents an itinerant system. Nonetheless, the applicability of the bond valence (BV) model to metallic systems and in particular to delocalized metal-metal bonds has recently been demonstrated [33–35]. Accordingly, we calculate bond valence sums (BVS) from our crystal structure solution to provide a rough estimate of the effective valence of the V species, which would be the one most the likely to engender magnetism in $Zr_3V_3GeSn_4$. In general, we calculate BVSs

from an estimated effective total site valence V_i of species i from the sum of the individual valences S_{ij} arising from bonds between species i and j as

$$V_i = \sum_j S_{ij} = e^{(R_0 - R_{ij})/b},$$

where R_{ij} are the experimentally determined bond lengths between species i and j, while both the bond softness b and the ideal bond length R_0 are empirically determined and typically tabulated constants. In our calculation, we consider four nearest-neighbor V-Sn2 bonds with distances 2.75791(16) Å, two next-nearest-neighbor V-V bonds with distances 2.78355(10) Å, and two next-next-nearest-neighbor Sn1 atoms with bond distances 3.00581(15) Å, which together form the polyhedron shown in Figure 1d. We take tabulated BV parameters for metal-metal V-V bonds to be $R_0 = 2.435$ Å and $b = 0.43$ Å [33]. To our knowledge, V-Sn BV parameters remain unavailable, so we take the known V-Te parameters $R_0 = 2.57$ Å and $b = 0.37$ Å as approximations given the similar atomic and single-bond covalent radii of Sn and Te. Our resulting estimated BVS for V in $Zr_3V_3GeSn_4$ is 3.9122(6), suggesting that V may effectively bond as a tetravalent species and therefore may host an effective spin-1/2 magnetic moment in this system. By way of comparison, β-Ti_6Sn_5 is a Pauli paramagnet with an effective spin-1/2 moment that arises only upon chemical doping and ordering [23,25]. Of course, magnetic measurements will be required clarify the nature of magnetism if any in $Zr_3V_3GeSn_4$.

5. Conclusions

$Zr_3V_3GeSn_4$ represents the second quaternary ordered derivative of β-Ti_6Sn_5 and the first containing V or Ge, though solid solutions of the known isostructural binaries V_6Sn_5, Ta_6Ga_5, and $Ti_6Pb_{4.8}$ have also been reported [27]. The recent discovery of two quaternary ordered derivatives suggests that yet more undiscovered compounds exist with this structure-type.

Most interestingly, the sites most likely to host 3*d*-based magnetic character (V in $Zr_3V_3GeSn_4$ and Mn in $Zr_3Mn_3Sn_4Ga$) are arranged in one-dimensional chains along the crystallographic **c**-axis, with the chains themselves arranged in a kagome geometry.Though no magnetic studies on this class of materials have thus far appeared in the literature, these systems may offer an opportunity to study the interplay of low-dimensionality and magnetic frustration in 3*d* transition metal systems. Moreover, estimated BVS calculations in $Zr_3V_3GeSn_4$ suggest that V could take an effective spin-1/2 configuration, which could lead to quantum fluctuations and perhaps novel emergent phenomena.

Author Contributions: Conceptualization, design, D.P. and J.W.S.; synthetic development, D.P.; X-ray measurements, J.W.S. All authors contributed to data analysis, and all authors contributed to writing the manuscript. All authors have read and agreed to the published version of the manuscript.

Funding: The Stony Brook University single crystal diffractometer was obtained through the support of the National Science Foundation grant CHE-0840483. D. Parks was supported in part by the Blind Pig Foundation. J. W. Simonson was supported in part by a Provost's Research Fellowship from Farmingdale State College.

Data Availability Statement: The data presented in this study are openly available in the Crystallography Open Database, entry number 3000436.

Conflicts of Interest: The authors declare no conflict of interest. The funders had no role in the design of the study; in the collection, analyses, or interpretation of data; in the writing of the manuscript; or in the decision to publish the results.

Abbreviations

The following abbreviations are used in this manuscript:

ADP	Anisotropic displacement parameter
BV	Bond valence
BVS	Bond valence sum
CCD	Charge-coupled device
DFT	Density functional theory
FM	Ferromagnetic
QCP	Quantum critical point

References

1. Wickramaratne, D.; Khmelevskyi, S.; Agterberg, D.F.; Mazin, I.I. Ising Superconductivity and Magnetism in $NbSe_2$. *Phys. Rev. X* **2020**, *10*, 041003. [CrossRef]
2. Simonson, J.W.; Yin, Z.P.; Pezzoli, M.; Guo, J.; Liu, J.; Post, K.; Efimenko, A.; Hollman, N.; Hu, Z.; Lin, H.-J.; et al. From antiferromagnetic insulator to correlated metal in pressurized and doped LaMnPO. *Proc. Nat. Acad. Sci.* **2012**, *109*, E1815–E1819. [CrossRef] [PubMed]
3. Jourdan, M.; Minár, J.; Braun, J.; Kronenberg, A.; Chadov, S.; Balke, B.; Gloskovskii, A.; Kolbe, M.; Elmers, H.J.; Schönhense, G.; et al. Direct observation of half-metallicity in the Heusler compound Co_2MnSi. *Nat. Commun.* **2014**, *5*, 3974. [CrossRef]
4. Miiller, W.; Wu, L.S.; Kim, M.S.; Orvis, T.; Simonson, J.W.; Gamża, M.; McNally, D.M.; Nelson, C.S.; Ehlers, G.; Podlesnyak, A.; et al. Magnetic structure of Yb_2Pt_2Pb: Ising moments on the Shastry-Sutherland lattice. *Phys. Rev. X* **2016**, *93*, 104419. [CrossRef]
5. Uhlarz, M.; Pfleiderer, C.; Hayden, S.M. Quantum Phase Transitions in the Itinerant Ferromagnet $ZrZn_2$. *Phys. Rev. Lett.* **2004**, *93*, 256404. [CrossRef]
6. Chen, W.; James, A.D.N.; Dugdale, S.B. Local electron correlation effects on the fermiology of the weak itinerant ferromagnet $ZrZn_2$. *Electron. Struct.* **2022**, *4*, 045002. [CrossRef]
7. Aguayo, A.; Singh, D.J. Itinerant ferromagnetism and quantum criticality in Sc_3In. *Phys. Rev. B* **2002**, *66*, 020401(R). [CrossRef]
8. Fei, Z.; Huang, B.; Malinowski, P.; Wang, W.; Song, T.; Sanchez, J.; Yao, W.; Xiao, D.; Zhu, X.; May, A.F.; et al. Two-dimensional itinerant ferromagnetism in atomically thin Fe_3GeTe_2. *Nat. Mater.* **2018**, *17*, 778–782. [CrossRef]
9. de la Barrera, S.C.; Aronson, S.; Zheng, Z.; Watanabe, K.; Taniguchi, T.; Ma, Q.; Jarillo-Herrero, P.; Ashoori, R. Cascade of isospin phase transitions in Bernal-stacked bilayer graphene at zero magnetic field. *Nat. Phys.* **2022**, *18*, 771–775. [CrossRef]
10. Huang, C.-L.; Hallas, A.M.; Grube, K.; Kuntz, S.; Spielß, B.; Bayliff, K.; Besara, T.; Siegrist, T.; Cai, Y.; Beare, J.; et al. Quantum Critical Point in the Itinerant Ferromagnet $Ni_{1-x}Rh_x$. *Phys. Rev. Lett.* **2020**, *124*, 117203. [CrossRef]
11. Luo, J.; Yang, J.; Zhou, R.; Mu, Q.G.; Liu, T.; Ren, Z.-A.; Yi, C.J.; Shi, Y.G.; Zheng, G.-Q. Tuning the Distance to a Possible Ferromagnetic Quantum Critical Point in $A_2Cr_3As_3$. *Phys. Rev. Lett.* **2020**, *123*, 047001. [CrossRef] [PubMed]
12. Mishra, A.K.; Shanmukharao S.S.; Lees, M.R.; Ganesan, V. Disorder-induced critical exponents near a ferromagnetic quantum critical point in $Mn_{1-x}Cr_xSi$. *Phys. Rev. B* **2020**, *101*, 144436. [CrossRef]
13. Taufour, V.; Kaluarachchi, U.S.; Khasanov, R.; Nguyen, M.C.; Guguchia, Z.; Biswas, P.K.; Bonfà, P.; De Renzi, R.; Lin, X.; Kim, S.K.; et al. Ferromagnetic Quantum Critical Point Avoided by the Appearance of Another Magnetic Phase in $LaCrGe_3$ under Pressure. *Phys. Rev. Lett.* **2016**, *117*, 037207. [CrossRef] [PubMed]
14. Xiang, L.; Gati, E.; Bud'ko, S.L.; Saunders, S.M.; Canfield, P.C. Avoided ferromagnetic quantum critical point in pressurized $La_5Co_2Ge_3$. *Phys. Rev. B* **2021**, *103*, 054419. [CrossRef]
15. Gati, E.; Wilde, J.M.; Khasanov, R.; Li, X.; Dissanayake, S.; Gupta, R.; Matsuda, M.; Ye, F.; Haberl, B.; Kaluarachchi, U.; et al. Formation of short-range magnetic order and avoided ferromagnetic quantum criticality in pressurized $LaCrGe_3$. *Phys. Rev. B* **2021**, *103*, 075111. [CrossRef]
16. Iwahara, R.; Sugawara, R.; Rahmanto; Honma, Y.; Matsuoka, K.; Matsuo, A.; Kindo, K.; Tenya, K.; Yokoyama, M. Avoided quantum criticality and cluster-glass formation in itinerant ferromagnet $Sr_{1-x}(La_{0.5}K_{0.5})_xRuO_3$. *Phys. Rev. Mater.* **2020**, *4*, 074404. [CrossRef]
17. Benka, G.; Bauer, A.; Schmakat, P.; Säubert, S.; Seifert, M.; Jorba, P.; Pfleiderer, C. Interplay of itinerant magnetism and spin-glass behavior in Fe_xCr_{1-x}. *Phys. Rev. Mater.* **2022**, *6*, 044407. [CrossRef]
18. Kirkpatrick, T.R.; Belitz, D. Ferromagnetic Quantum Critical Point in Noncentrosymmetric Systems. *Phys. Rev. Lett.* **2020**, *124*, 147201. [CrossRef]
19. Pietrokowsky, P.; Frink, E.P. A constitution diagram for the alloy system titanium tin. *Trans. Am. Soc. Met.* **1957**, *49*, 339–358.
20. Schubert, K; Frank, K.; Gohle, R.; Maldonado, A.; Meissner, H.G.; Raman, A.; Rossteutscher, W. Einige Strukturdaten metallischer Phasen (8). *Naturwissenschaften* **1963**, *50*, 41–41. [CrossRef]
21. Gandova, V.; Petrova, I. New thermodynamic investigation of some solid phases of Sn-Ti phase diagram. *IOP Conf. Ser. Mater. Sci. Eng.* **2020**, *878*, 012068. [CrossRef]
22. Oni, A.A.; Hook, D.; Maria, J.P.; LeBeau, J.M. Phase coexistence in Ti_6Sn_5 intermetallics. *Intermetallics* **2014**, *51*, 48–52. [CrossRef]
23. Drymiotis, F.; Lashley, J.C.; Fisk, Z.; Peterson, E.; Nakatsuji, S. Physical properties of the β-Ti_6Sn_5 system. *Phil. Mag.* **2003**, *83*, 3169–3178. [CrossRef]

24. Kordan, V.; Zelinska, O.; Pavlyuk, V.; Oschchapovsky, I.; Serkiz, R. Electrochemical lithiation of Ti_5M_3, Ti_3M and Zr_3M (M = Sn, Sb) binary intermetallics. *Chem. Met. Alloys* **2016**, *9*, 84–91. [CrossRef]
25. Jeong, T. Electronic structure and magnetic properties of β-Ti_6Sn_5. *J. Magn. Magn. Mater.* **2007**, *309*, 71–74. [CrossRef]
26. Linsinger, S.; Pöttgen, R. Chains of Condensed $RuSm_{6/2}$ Octahedra in Sm_3RuMg_7—A Ternary Ordered Version of the Ti_6Sn_5 Type. *Z. Naturfosch.* **2011**, *66b*, 565–569.
27. Clausse T.; Diop, L. V. B.; Martin, N. P.; Sibille, R.; Mazet, T. $Zr_3Mn_3Sn_4Ga$: A new hexagonal Ti_6Sn_5-type quaternary intermetallic. *Acta Cryst.* **2022**, *B78*, 817–822. [CrossRef]
28. Clark, R.C.; Reid, J.S. The analytical calculation of absorption in multifaceted crystals. *Acta Cryst.* **1995**, *A51*, 887–897. [CrossRef]
29. Petricek, V.; Dusek, M.; Palatinus, L. Crystallographic Computing System JANA2006: General features. *Z. Kristallogr.* **2014**, *229*, 345–352. [CrossRef]
30. Palatinus L.; Chapuis G. Superflip—A computer program for the solution of crystal structures by charge flipping in arbitrary dimensions. *J. Appl. Cryst.* **2007**, *40*, 786–790. [CrossRef]
31. Momma, K.; Izumi, F. VESTA 3 for three-dimensional visualization of crystal, volumetric and morphology data. *J. Appl. Crystallogr.* **2011**, *44*, 1272–1276. [CrossRef]
32. Becker, P.J.; Coppens, P. Extinction within the limit of validity of the Darwin transfer equations. III. Non-spherical crystals and anisotropy of extinction. *Acta Cryst.* **1975**, *A31*, 417–425. [CrossRef]
33. Levi, E.; Aurbach, D.; Gatti, C. Bond Order Conservation Principle and Peculiarities of the Metal-Metal Bonding. *Inorg. Chem.* **2018**, *57*, 15550–15557. [CrossRef] [PubMed]
34. Levi, E.; Aurbach, D.; Gatti, C. A revisit of the bond valence model makes it universal. *Phys. Chem. Chem. Phys.* **2020**, *22*, 13839–13849. [CrossRef]
35. Levi, E.; Aurbach, D.; Gatti, C. Metal–Metal Bond in the Light of Pauling's Rules. *Molecules* **2021**, *26*, 304. [CrossRef]

Disclaimer/Publisher's Note: The statements, opinions and data contained in all publications are solely those of the individual author(s) and contributor(s) and not of MDPI and/or the editor(s). MDPI and/or the editor(s) disclaim responsibility for any injury to people or property resulting from any ideas, methods, instructions or products referred to in the content.